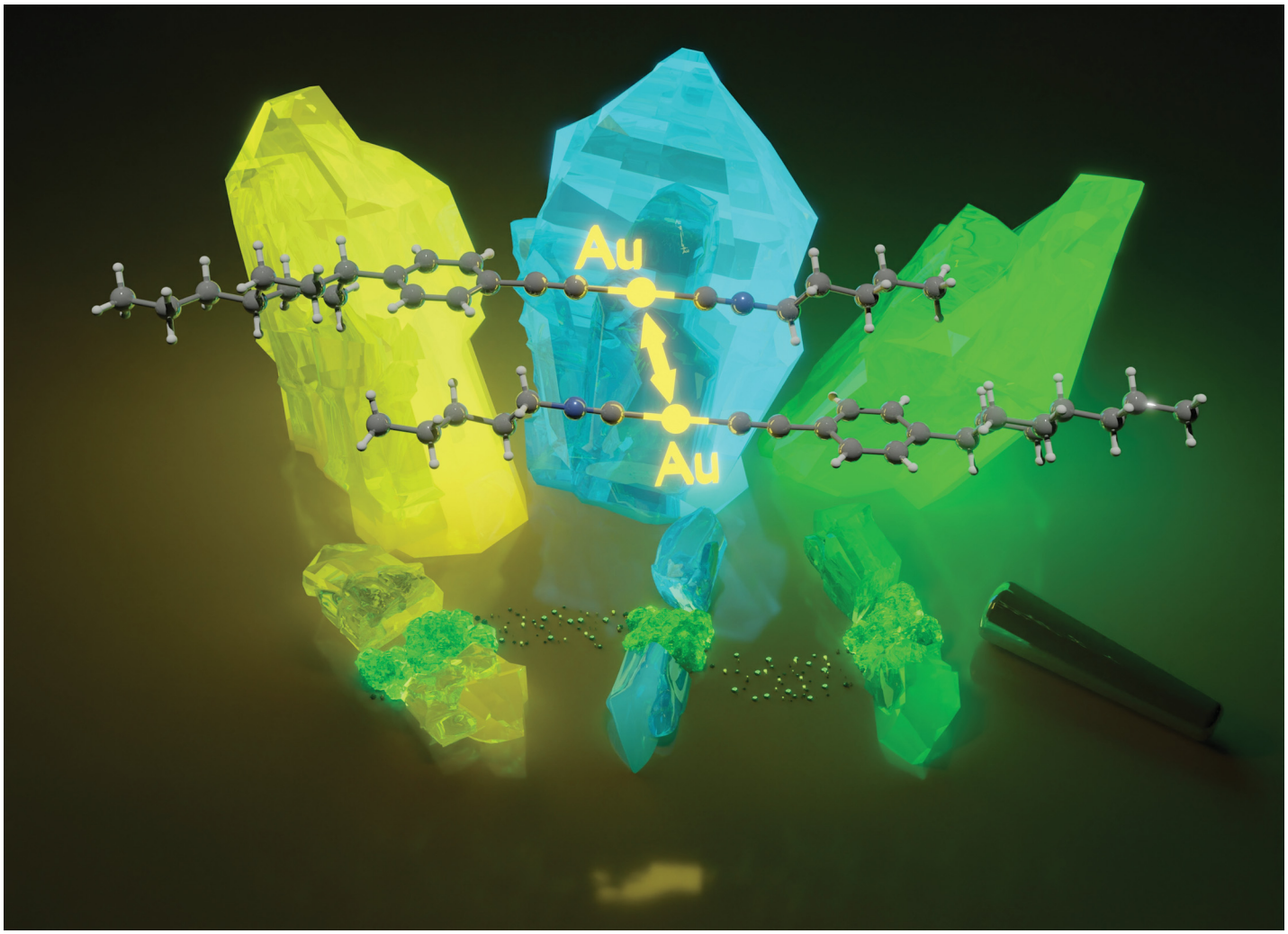

Showcasing research from Professor Tsutsumi's laboratory, Department of Applied Chemistry, Ritsumeikan University, Kusatsu, Japan.

Tricolour luminescence in an Au(I) complex controlled by polymorphism and mechanical stress

A rod-like Au(I) complex, **CP**, featuring a cyclohexylphenyl moiety and an isocyanide ligand, exhibited tricolour luminescence attributable to polymorphism. Mechanical stimuli, which alter the aggregated structure, can induce a switch in its luminescence colour. Additionally, the **CP** Au(I) complex displayed a liquid-crystalline (LC) phase wherein luminescence was observed. Our study demonstrates that the luminescence behaviour of the **CP** Au complex can be effectively controlled through crystalline-to-crystalline and crystalline-to-LC phase transitions.

As featured in:

See Osamu Tsutsumi *et al.*, *Mater. Adv.*, 2024, **5**, 5052.

ROYAL SOCIETY OF CHEMISTRY

rsc.li/materials-advances

Registered charity number: 207890

Materials Advances

ROYAL SOCIETY OF CHEMISTRY

PAPER

View Article Online
View Journal | View Issue

Cite this: *Mater. Adv.*, 2024, 5, 5052

Tricolour luminescence in an Au(I) complex controlled by polymorphism and mechanical stress†

Andriani Furoida, Misato Daitani, Kohsuke Matsumoto, Kyohei Hisano ‡ and Osamu Tsutsumi *

The aggregation-induced emission (AIE) behaviour of gold(I) complexes has been extensively reported. In particular, Au complexes that exhibit colour tunability towards changes in aggregated structures are becoming increasingly attractive in the field of materials science. Herein, we report **CP**, a rod-shaped Au complex with a cyclohexylphenyl moiety and an isocyanide ligand. The photophysical behaviour of **CP** in various states is discussed based on their primary and aggregated structures. **CP** emitted room-temperature phosphorescence (RTP) with high-contrast polymorph-dependent colours of blue (**CP-B**), green (**CP-G**), and yellow (**CP-Y**) depending on the recrystallisation conditions. **CP-Y**, which has the shortest Au–Au distance, exhibits an efficient direct S_0–T_n transition, leading to an enhanced RTP quantum yield (Φ_{RTP}) of 38% under S_0–T_n excitation. Interestingly, X-ray diffraction analysis revealed that **CP-B** and **CP-G** exhibit identical crystal structures despite their distinct emission colours. Photophysical and differential scanning calorimetry analyses revealed that the presence of small crystal domains, such as those in the ground samples of **CP**, is responsible for the overall green emission observed in bulk **CP-G**, indicating that the crystal structure and size determine the RTP colour. Moreover, **CP** also exhibits a liquid-crystalline (LC) nature and mechanochromic luminescence. Our findings demonstrate that the aggregated structure and AIE properties of Au complexes can be effectively controlled through crystalline-to-LC or crystalline-to-crystalline phase transitions of the complexes.

Received 26th March 2024,
Accepted 10th May 2024

DOI: 10.1039/d4ma00314d

rsc.li/materials-advances

Introduction

Organic materials showing bright luminescence in solid states have aroused increasing attention due to their potential applications in various light-emitting technologies, such as cell imaging, chemo-sensors, biosensors, and organic light-emitting devices.[1] However, the luminescence of typical organic chromophores is quenched in an aggregated state, posing a significant limitation for practical light-emitting applications where emission in aggregated states is imperative.[2] Over the past two decades, the pursuit of molecules with aggregation-induced emission (AIE) properties, characterized by a rotor-like structure that renders them non-emissive in dilute solution but strongly emissive in aggregated or solid states, has emerged as a vibrant area of research.[3]

The solid-state luminescence of organic materials is not only intricately linked to their molecular structure but also to their molecular packing and intermolecular interactions.[4] Thus, deliberate modulation of aggregated structures is crucial for tuning the luminescence properties of AIE materials. Recently, there has been a growing interest in materials exhibiting distinct solid-state luminescence properties from a single chromophore, capitalising on polymorphic behaviour. Polymorphic materials encompass multiple crystalline phases, each exhibiting a unique emission colour.[5] Notably, mechanochromic luminescence (MCL) has garnered considerable attention due to its broad applicability in sensors, probes, and memory devices. In such systems, mechanical forces (*e.g.*, grinding and stretching) induce significant changes in photophysical properties, primarily attributable to changes in the aggregated structure.[6] Another noteworthy approach to manipulate the aggregated structure is through the introduction of liquid-crystalline (LC) properties. The integration of LC properties into AIE materials imparts tunability to their luminescence properties through the control of molecular alignment *via* self-assembly and responsiveness to external fields.[7]

Department of Applied Chemistry, Ritsumeikan University, Kusatsu 525-8577, Japan. E-mail: tsutsumi@sk.ritsumei.ac.jp

† Electronic supplementary information (ESI) available. CCDC 2327717, 2327718 and 2327741. For ESI and crystallographic data in CIF or other electronic format see DOI: https://doi.org/10.1039/d4ma00314d

‡ Present address: Laboratory for Chemistry and Life Science, Institute of Innovative Research, Tokyo Institute of Technology, 4259 Nagatsuta, Midori-ku, Yokohama 226-8501, Japan.

Gold(I) complexes offer an attractive avenue in this pursuit, offering not only efficient luminescence in aggregated states but also stimuli-responsive luminescence behaviour owing to distinctive Au–Au (aurophilic) interactions. Indeed, numerous studies have reported various Au complexes with tuneable luminescent colours in response to external stimuli (*e.g.*, mechanical force, heat, and pressure).[8] An Au complex featuring a linear coordination geometry, reported to exhibit LC properties, enables control of molecular alignment *via* external stimuli and luminescence properties through the alternation of Au–Au distances.[9]

The combination of multicolour emission in polymorphic materials with controllable molecular alignment in LC molecules provides organic materials with multifunctional applications. However, the development of luminescent materials exhibiting both polymorphism and LC behaviour remains rare.[10] We have previously reported rod-like Au complexes bearing biphenylethynyl and isocyanide ligands that exhibit intense room-temperature phosphorescence (RTP) in aggregates. However, the observation of high-contrast luminescence coupled with polymorphism behavior and LC properties has proven elusive, likely due to the rigid structure of the biphenyl moiety.[11] In this study, we designed and synthesised a novel Au complex, **CP**, featuring a cyclohexylphenyl moiety and isocyanide ligands, as shown in Fig. 1. Due to the non-rigid structure of the cyclohexylphenyl moiety, the complex exhibited both LC properties and crystalline polymorphism. Intriguingly, **CP** yielded three distinct crystal forms with distinctive RTP colours (blue, green, and yellow) under various recrystallisation conditions. Among these polymorphs, the crystal emitting yellow light, **CP-Y**, displayed a relatively high RTP quantum yield (Φ) of 38%—even in the presence of air. In addition, **CP-B** (blue-emitting crystal) and **CP-G** (green-emitting crystal) shared an identical aggregated structure despite their disparate luminescence behaviours. Upon mechanical grinding of all **CP** crystals, a small crystal domain emitting green light was obtained. Moreover, luminescence was also apparent in the LC phase at high temperature (>100 °C) and the luminescent colour change was induced by a crystalline-to-LC phase transition. Our results strongly suggest that the aggregated structure and luminescence behaviour of **CP** can be readily controlled *via* crystal-to-crystal and crystal-to-LC phase transitions.

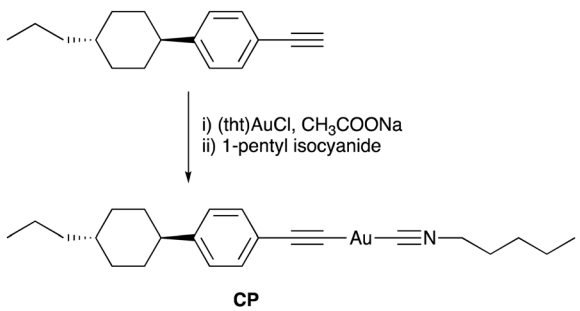

Fig. 1 Synthesis and molecular structure of the **CP** Au complex.

Results and discussion

Synthesis and characterization of the Au complex

The molecular structure of the Au complex used in this study is shown in Fig. 1. **CP** was prepared from commercially available 1-ethynyl-4-(*trans*-4-propylcyclohexyl)benzene in two facile steps: complexation with tetrahydrothiophene gold(I) chloride ((tht)AuCl), and subsequent ligand exchange with 1-pentyl isocyanide. The Au complex was successfully purified by silica gel column chromatography, followed by recrystallisation from a mixed solvent system of CH_2Cl_2 and hexane. The complex was characterised using ^{1}H NMR, ^{13}C NMR, infrared (IR) spectroscopy, high-resolution mass spectroscopy (HRMS), and elemental analysis. All the analytical data (provided in the Experimental section) confirmed that the desired Au complex was obtained in high purity.

The thermal stability of the Au complex was evaluated using thermogravimetric/differential thermal analysis (TG–DTA) at a heating rate of 5 °C min^{-1} in the range of 25–600 °C. The thermal decomposition temperature (T_{dec}) is defined as the temperature at which 5% weight loss occurs. As shown in Fig. S4 (ESI†), **CP** decomposed at approximately 186 °C. According to our previous study on the Au isocyanide complex, decomposition is initiated by the disconnection of the isocyanide ligand.[11] The calculated weight percentage of isocyanide ligands in the total weight of **CP** is 19%. Thus, the first weight loss of 18% is attributed to C–Au bond cleavage between the Au atom and the isocyanide ligand. The 37% residual ash corresponded to the calculated percentage of Au (37.9%), suggesting that the residue remaining after heating was in the form of Au ash. This result is also consistent with the ash percentage obtained from the elemental analysis of **CP** (see the Experimental section).

Photophysical properties in solution

The photophysical properties of **CP** were investigated in dilute solutions (Fig. 2). An absorption band at 288 nm with a molar extinction coefficient (ε) of 9.4 × 10^4 L mol^{-1} cm^{-1} was observed in CH_2Cl_2 solution (1 × 10^{-5} mol L^{-1}), which is

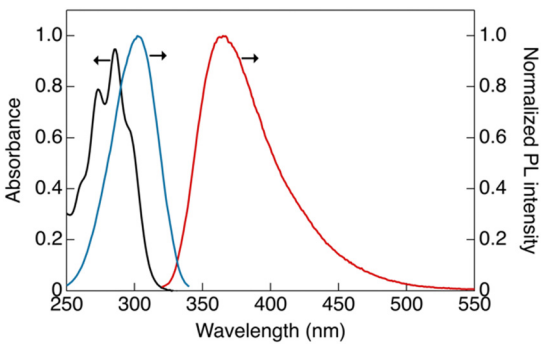

Fig. 2 Absorption and corrected photoluminescence spectra of **CP** in CH_2Cl_2 solution: black, absorption spectra ([**CP**] = 1 × 10^{-5} mol L^{-1}); red, luminescence spectra ([**CP**] = 1.5 × 10^{-6} mol L^{-1}, λ_{ex} = 302 nm); and blue, excitation spectra ([**CP**] = 1.5 × 10^{-6} mol L^{-1}, λ_{em} = 365 nm).

attributable to the ligand-base π–π* transition (Fig. 2, black line).[12]

The dilute solution of **CP** ([**CP**] = 1.5 × 10^{-6} mol L^{-1}) showed a single emission band at 365 nm (band I) under ambient conditions. In the excitation spectrum (Fig. 2, blue line), an excitation band was observed at wavelengths longer than those in the absorption spectrum. This marginal red-shift observed in the excitation band can be attributed to the formation of aggregates in the solution that are likely to be more emissive than the monomeric form of **CP**.[11] The luminescence decay at band I in the dilute solution was within the nanosecond region, indicating that the luminescence at this band is fluorescence (Fig. S9a, ESI†).

Similar luminescence was also obtained in a concentrated THF solution ([**CP**] = 1 × 10^{-4} mol L^{-1}). Upon the addition of water as a poor solvent to the THF solution, a gradual reduction in the luminescence intensity at 365 nm was observed until the volume fraction of water in the mixed solution (f_w) reached 60% (Fig. 3). Beyond an f_w value of 60%, two distinctive emission bands emerged abruptly at 424 (band II) and 500 nm (band III), indicating the formation of aggregates. Consequently, the overall luminescence intensity of **CP** in the mixed solvent increased significantly (Fig. 3c), confirming the AIE-active nature of the synthesised Au complex. The reduction in the total luminescence intensity in the $f_w > 80\%$ range is not indicative of the ACQ effect, but rather arises from precipitation due to the formation of relatively large crystals.

To investigate the emission origins of bands II and III, we initially observed the luminescence in a dilute THF/water solution ([**CP**] = 1.5 × 10^{-6} mol L^{-1}) under an Ar atmosphere (Fig. S8a, ESI†). At f_w = 0%, which initially showed only band I, a pronounced shift towards band II was observed under Ar, indicating that band II corresponded to monomeric phosphorescence. In contrast, a weak band III appeared at f_w = 80% under Ar, indicating that the phosphorescence originated from the aggregates.

Luminescence lifetime (τ) measurements in the solution under Ar also supported the emission origin of these three bands. As shown in Fig. S9 and Table S3 (ESI†), bands I and II exhibited nanosecond-scale lifetimes in ambient air. Under Ar, the emission lifetime of band II was significantly increased to the microsecond scale, whereas no significant change was observed in the lifetime of band I. This provides evidence that the observed luminescence at band I can be attributed to fluorescence, and that band II corresponds to phosphorescence. Additionally, as shown in Fig. S9a (ESI†), a rise in the fluorescence intensity of band I was observed during the lifetime measurement. This suggests that the fluorescence of band I originates from an excimer.

In contrast, band III showed biexponential decay with a microsecond-scale lifetime in both air and Ar atmospheres (Fig. S10b and Table S3, ESI†). Because the emission from band III arose from the aggregates, this band was negligible in dilute solutions. We also observed luminescence in a more concentrated solution ([**CP**] = 1 × 10^{-5} mol L^{-1}) (Fig. S8b, ESI†). Similar results to those obtained in the dilute solution

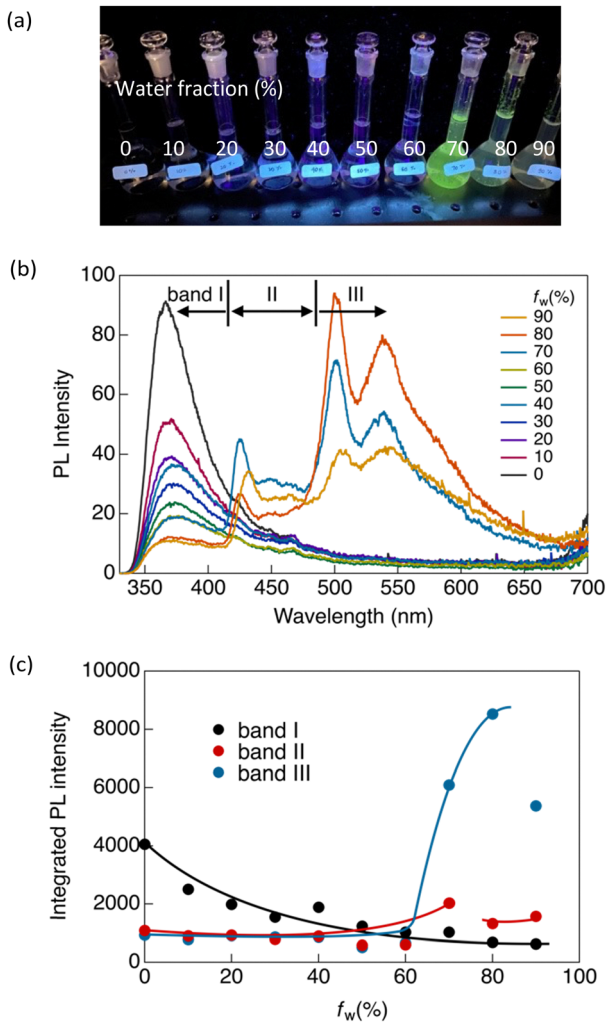

Fig. 3 (a) Photograph of **CP** in a THF/water mixed solvent (f_w = 0–90%) under UV irradiation at 365 nm. (b) Emission spectra of **CP** in f_w = 0–90% ([**CP**] = 1 × 10^{-4} mol L^{-1}, λ_{ex} = 300 nm). (c) Integrated photoluminescence intensity in different wavelength ranges: band I, 330–420 nm; band II, 420–480 nm; and band III, 480–700 nm.

(10^{-6} mol L^{-1}) were observed at f_w = 0%. However, unlike the dilute solution, at f_w = 80%, band III is clearly visible even in the presence of air. This indicated that **CP** formed more aggregates at high concentrations. This aggregated emission was further amplified and became predominant at f_w = 80% under an inert atmosphere, accompanied by an extended lifetime on the microsecond scale (Fig. S10b and Table S3, ESI†). This indicates that band III corresponds to phosphorescence originating from aggregates, and therefore, that **CP** exhibits aggregation-induced phosphorescence.

In our previous study, we demonstrated that the stability of the crystal structures in certain gold(I) complexes depends on crystal size, with crystal-to-crystal phase transitions occurring at critical sizes during crystal growth.[13] The present study on **CP** reveals phenomena similar to those of the previously reported system, in which a crystal-to-crystal phase transition occurs during the crystal growth process in a mixed solvent.

Initially, crystal nuclei, corresponding to band II, are formed upon the addition of water. At a higher water fraction (f_w > 60%), crystals grew to the critical size, triggering a crystal-to-crystal phase transition and giving rise to band III. We attribute bands II and III to crystals of different sizes, and their formation strongly depends on water content. As shown in Fig. 3c, the ratio of the emission intensities of bands II and III changes as the water content increases. Bands II and III emerged simultaneously at f_w > 60%. The intensity of band II peaked at f_w = 70% and gradually decreased above this water fraction, whereas the relative emission intensity of band III decreased significantly after f_w > 80%. This implies a decrease in the number of small crystal nuclei (associated with the origin of band II) due to the formation of larger crystals (associated with the origin of band III) during the crystal growth process. Larger crystals (band III) predominate at higher water contents; however, they partially precipitate after f_w > 80%. This observation aligns with our previous research, where the crystal structures of Au complexes as well as their luminescence properties were contingent on crystal size.[13]

Luminescence properties of the complex in bulk crystals

CP exhibit intriguing luminescence properties in bulk crystals. By controlling the recrystallisation conditions, three types of plate-like crystals exhibiting different luminescent colours (blue, green, and yellow) were successfully obtained. Rapid and slow evaporation of a solvent mixture of CH_2Cl_2 and hexane (1 : 3 v/v) afforded blue-emitting **CP-B** and green-emitting **CP-G**, respectively. **CP-Y**, which emits yellow light, was obtained *via* slow recrystallisation from a mixture of CH_2Cl_2 and ethyl acetate (1 : 3 v/v). Recrystallisation from a mixture of CH_2Cl_2 and hexane (2 : 1 v/v) afforded a mixture of **CP-Y** and **CP-B** crystals. As shown in Fig. 4, **CP-B** and **CP-G** exhibited vibronic emission bands, with maxima at 423 and 500 nm, respectively, while **CP-Y** showed an emission band peaked at 560 nm without a vibronic structure. In comparison to luminescence in solution, the solid-state emissions were red-shifted, suggesting that the luminescence arises from lower-energy triplet excited states.[14] Similar emission bands at 423 and ~500 nm were also observed in the degassed THF/water solution, further substantiating that these emissions correspond to phosphorescence.

In our previous study, we investigated the luminescence behaviour of Au complexes with similar molecular structures.[9a,15] What distinguishes **CP** from the previously reported complex is the structure of the acetylide ligand: **CP** utilises a cyclohexylphenylacetylide ligand instead of a phenylacetylide ligand. Interestingly, the phenylacetylide Au complex did not exhibit any crystalline polymorphism and emitted blue light, similar to **CP-B** in its crystalline phase. The introduction of a cyclohexyl group in **CP** played a crucial role in inducing crystal polymorphism and a diverse range of luminescent colours. Our findings suggest the capability of tuning the emission wavelength across a wide range of the visible spectrum, from blue to yellow, in Au complex systems without extending the π-conjugation system.

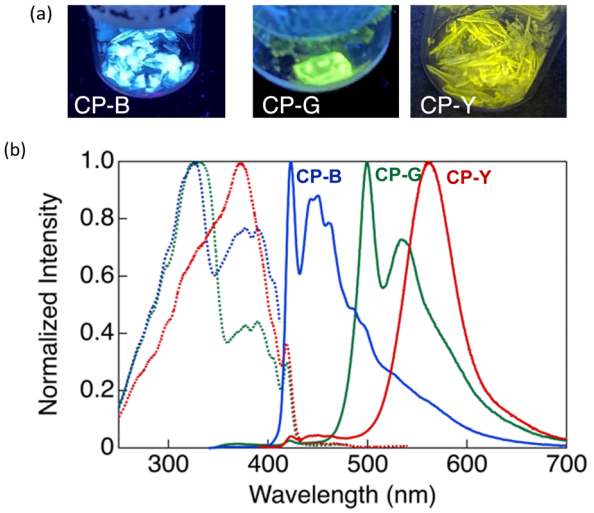

Fig. 4 (a) Photographs of crystal polymorphs of **CP-B**, **CP-G**, and **CP-Y** under UV irradiation at 365 nm. (b) Excitation (dashed lines) and emission (solid lines) spectra of the **CP** crystal polymorphs: **CP-B** (blue, λ_{ex} = 320 nm for excitation, λ_{em} = 423 nm for emission); **CP-G** (green, λ_{ex} = 320 nm, λ_{em} = 500 nm); and **CP-Y** (red, λ_{ex} = 320 nm, λ_{em} = 560 nm).

As shown in Fig. 4, **CP-B** and **CP-G** exhibited similar excitation spectra, with a primary excitation band at approximately 320 nm, which was also observed in the absorption spectra of the solutions and is attributable to the S_0–S_n transition.[15] An additional excitation band was observed at longer wavelengths (370–420 nm). We have previously reported that this excitation band is due to an S_0–T_n direct transition that is strictly spin-forbidden.[15] However, in this type of rod-like Au complex, an extremely efficient S_0–T_n direct transition occurs due not only to the heavy atom effect but also to Au–Au interactions formed by the aggregation of the Au complex.[15] The excitation spectra of **CP-Y** are distinct compared to other polymorphs, with the maxima at 373 nm and a shoulder peak at ~320 nm. Among the three polymorphs, **CP-Y** showed an efficient S_0–T_n transition, where the luminescence quantum yields (Φ) increased from 33% when excited at 320 nm (S_0–S_n transition) to 38% upon excitation at 373 nm (S_0–T_n transition) (Fig. 5 and Table 1). This result is in accordance with our

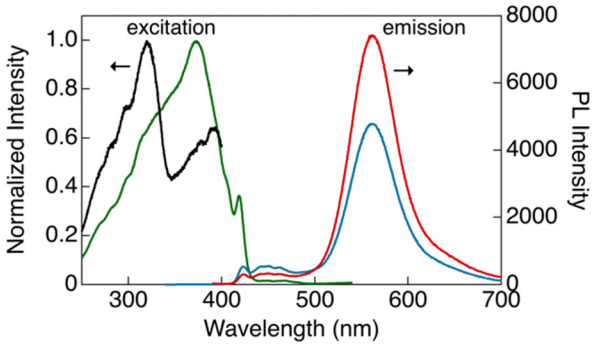

Fig. 5 Excitation (black, λ_{em} = 423 nm; green, λ_{em} = 560 nm) and emission (blue, λ_{ex} = 320 nm; red: λ_{ex} = 373 nm) spectra of **CP-Y** in bulk crystals at room temperature.

Table 1 Photophysical parameters of **CP** crystal polymorphs[ab]

	λ_{max}^{lum} (nm)	Φ	τ (μs)	k_r[c] (s^{-1})	k_{nr}[c] (s^{-1})
CP-B	423	0.10	11 (50%) 27 (50%)	5.2×10^3	4.7×10^4
CP-G	500	0.23	4 (52%) 389 (48%)	1.2×10^3	4.0×10^3
CP-Y	560	0.33 0.38[d]	13	2.9×10^4	4.7×10^4
Ground	500	5×10^{-3}	1 (86%) 16 (14%)	1.6×10^3	3.5×10^5

[a] Abbreviations: λ_{max}^{lum}, luminescence maxima; Φ, luminescence quantum yield; τ, luminescence lifetime; k_r, rate constant for radiative transition; k_{nr}, rate constant for non-radiative transition. [b] λ_{ex} = 320 nm for all measurements. [c] k_r was estimated as Φ/τ and k_{nr} was estimated as $(1 - \Phi)/\tau$; the weighted average of τ was used to estimate k_r and k_{nr}. [d] Observed by direct S_0–T_n excitation at 373 nm.

previous work wherein direct excitation to the excited triplet state enhanced the Φ value for RTP.[15] This RTP enhancement was not observed in **CP-B** and **CP-G** (Fig. S11, ESI†), indicating that the S_0–T_n transition was less efficient for these polymorphs.

To gain a better understanding of the photophysical properties of **CP**, we investigated the photoluminescence τ and Φ of bulk crystal polymorphs (Table 1 and Fig. S12, ESI†). The three polymorphs exhibit biexponential decay profiles with lifetimes on the order of microseconds, indicating that the luminescence from the crystals is phosphorescence. Despite displaying phosphorescence, the **CP** polymorphs exhibited considerably good Φ values of up to 38% at room temperature. Generally, it is difficult to demonstrate phosphorescence emission with high Φ under ambient conditions because the triplet excited states tend to be deactivated by molecular oxygen and the thermal motions of the molecules. The strong RTP of the crystal is attributed not only to heavy atom effects but also to the crystallisation-induced phosphorescence due to the densely packed crystal which prevented the penetration of molecular oxygen from quenching the triplet excited states.[16] Furthermore, based on the Φ and τ values, the rate constants for radiative transition (k_r) and non-radiative deactivation (k_{nr}) of the complexes in the crystal were estimated. As summarised in Table 1, the large k_r value observed for **CP-Y** is responsible for its highest Φ value among the studied polymorphs. **CP-B** and **CP-G** have similar k_r values, and their Φ depends on k_{nr}.

Furthermore, we considered whether the luminescence observed in the crystal was thermally activated delayed fluorescence (TADF). We conducted temperature-dependent photoluminescence analyses of the crystal polymorphs (Fig. S13–S15, ESI†). All polymorphs exhibited obvious RTP behaviour, where the photoluminescence intensity gradually increased with decreasing temperature; the emission maxima at 77 K were approximately twice those at 290 K. Thus, the occurrence of TADF can be excluded from the crystal emission. In addition, the emission enhancement upon direct S_0–T_n excitation, which was not observed for **CP-B** or **CP-G** at room temperature, was observed at 77 K. The emission intensities of **CP-B** and **CP-G** under direct S_0–T_n excitation (373 nm) at 77 K were twice that under S_0–S_n excitation (320 nm). The triplet state was stabilised at low temperatures by a reduction in molecular motion, leading to an efficient S_0–T_n transition.[17] Notably, the **CP-G** crystal displayed enhanced emission upon being warmed back to room temperature (298 K) from 77 K under direct S_0–T_n excitation at 373 nm, a phenomenon not previously observed during cooling and subsequent heating cycles. This suggests that the cooling to 77 K induced morphological or structural changes in **CP-G** that persisted upon rewarming to 298 K, thereby enabling efficient direct S_0–T_n excitation at room temperature.

The crystal polymorphs were subjected to single-crystal X-ray diffraction (SCXRD) analysis at room temperature to clarify their structures. Typically, polymorphic materials with distinct luminescence properties have different aggregated structures.[5] All **CP** polymorphs crystallized in the triclinic *P*-1 space group with an anti-parallel orientation, and their Au–Au distances were within the range of 3.7 and 4.0 Å (Fig. 6a). Interestingly, **CP-B** and **CP-G** share nearly identical crystal structures, with similar intermolecular interactions, including an Au–Au distance of approximately 4.0 Å. The occurrence of such polymorphic behaviour is rare, and we discuss this intriguing phenomenon further in the following section. **CP-Y** possess a distinct crystal structure with a shorter Au–Au distance than the other polymorphs (~3.7 Å), which explains the observed difference in emission colour. As previously reported, an Au isocyanide complex with a short Au–Au distance (~3.5 Å) exhibited RTP enhancement upon excitation at the S_0–T_n region.[15] Similarly, the densely packed structure of **CP-Y** enables the efficient stabilisation of triplet excitations and S_0–T_n transition compared to the other polymorphs, leading to enhanced emission upon excitation in the S_0–T_n region. In addition, the CH–Au interaction is likely contributed to the crystal packing structure as the distance between the Au and H atom of the phenyl group is short (~2.9 Å; Fig. S3, ESI†).[18]

To study the electronic transitions in the present complex, we conducted a computational study using time-dependent density functional theory (TD-DFT) calculations. The B3LYP hybrid functional with the SDD and 6-311+G(d,p) basis sets for the Au and other atoms, respectively, was employed. Calculations were performed for the dimer of the **CP** polymorphs, whose structures were determined by SCXRD. The oscillator strength (*f*) distribution was calculated for the transition to the singlet excited state (Table S5, ESI†).

We selected molecular orbitals with large *f* values corresponding to the allowed electronic transitions from the singlet excited states (Fig. 6b for **CP-B** and Fig. S17–S18 for **CP-G** and **CP-Y**, ESI†). In Fig. 6b, the excitation at 319 nm in **CP-B** was attributed to the S_0–S_1 transition with a large *f* value of 0.5492. The electron density distribution from HOMO−1 to LUMO reveals that this electronic transition arises from the π orbital of the phenylethynyl ligand to the Au–Au atoms in neighbouring molecules. Consequently, it was assigned to the LMMCT transition, indicating the presence of aurophilic interactions within the crystal structure despite the Au–Au distances slightly exceeding the theoretical range, in accordance with

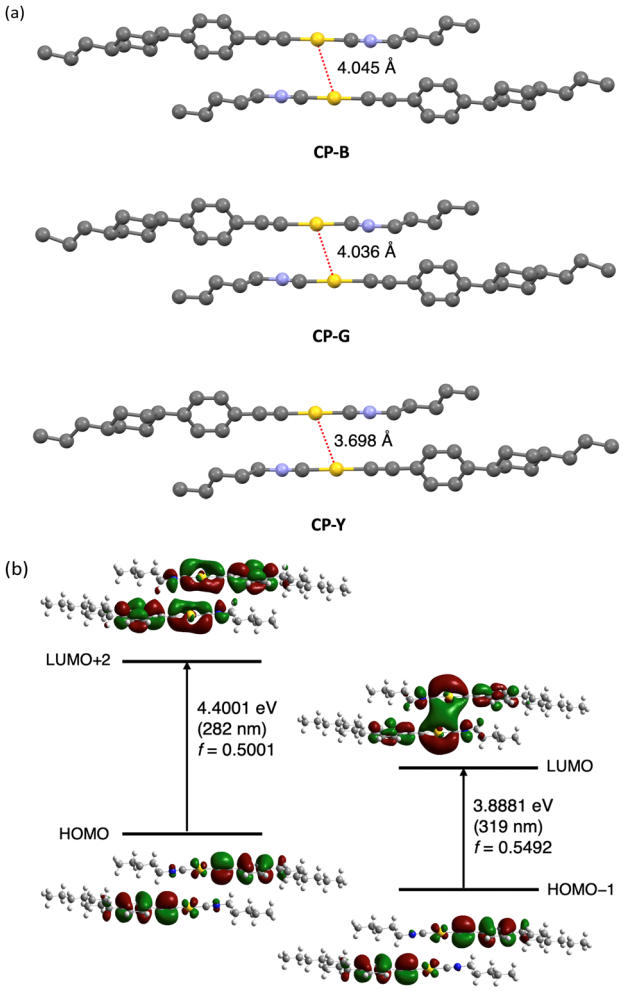

Fig. 6 (a) Single-crystal structure of **CP** polymorphs. Intermolecular Au–Au interactions are indicated with a dashed red line. Hydrogen atoms are omitted for clarity. Atom colour legend: grey, C; blue, N; yellow, Au. (b) Molecular orbitals of the **CP-B** dimer (extracted from the crystal structure) obtained from DFT calculation using B3LYP and 6-311+G(d,p), except for Au atoms, for which the SDD basis set was employed.

our previous finding.[11] The excitation at 282 nm, attributed to S_0–S_n, exhibited a high f value of 0.5001. According to the electron density distribution from the HOMO to LUMO+2, this transition arises from the π orbital of the phenylethynyl ligand to the Au atom within a single molecule. Thus, this transition was assigned as a ligand-to-metal charge transfer (LMCT) transition within the monomeric unit. Similar outcomes have been observed for other **CP** polymorphs, and these calculation results are closely aligned with the excitation observed in the crystal. In addition, the excitation energies of the triplet excited states were calculated from the same dimers, indicating that the S_0–T_1 transitions are located at 409, 372, and 412 nm for **CP-B**, **CP-G**, and **CP-Y**, respectively (Table S6, ESI†). The calculated excitation energy for the S_0–T_n transition was consistent with the longer excitation wavelength (370–420 nm) observed in the excitation spectra (Fig. 4b) for the **CP** crystal polymorphs. In the case of the monomer, the S_0–S_n transitions are located at 274 and 347 nm (Table S7, ESI†), which aligns with the absorption spectra of the complex in dilute solution (Fig. 2). Furthermore, the calculations suggested that an intramolecular LMCT transition occurred in the monomer (Fig. S19, ESI†).

Mechanochromic responsive properties

Given the observed correlation between the emission colour of **CP** and its crystal size during the crystal growth process, we investigated the luminescence behaviour of microsized **CP** crystals by applying mechanical stimuli (Fig. 7). SEM images of the ground crystals are shown in Fig. S21 (ESI†). Strong grinding of **CP-B** and **CP-Y** bulk crystals to microsized crystals induced a substantial emission colour change to green and bluish green, respectively. In the photoluminescence spectra, an obvious red-shift of the emission maxima from 423 to 500 nm was observed for ground **CP-B** (Fig. S20a, ESI†). In contrast, a blue-shifted emission from 560 to 469 nm was observed in ground **CP-Y** (Fig. S20c, ESI†). Although the emission maxima were different, ground **CP-B** and **CP-Y** exhibited similar broad low-intensity luminescence ranging from 350 to 700 nm. This emission colour change is typical of MCL behaviour and may be attributed to the alteration of the crystal arrangement upon mechanical grinding. Conversely, **CP-G** did not exhibit prominent MCL, and the emission colour remained green upon grinding. The luminescence intensity of **CP-G** decreased slightly, whereas the spectral shape was retained relative to that of the bulk crystals (Fig. S20b, ESI†). Despite the absence of emission spectral changes in ground **CP-G**, its excitation spectrum was identical to those of ground **CP-B** and **CP-Y**, suggesting that the luminescence originated from the same excited state (Fig. S20d, ESI†). As summarised in Table 1, the Φ of ground crystals decreased to ~0.5%, which is significantly lower compared to that in bulk crystals. Moreover,

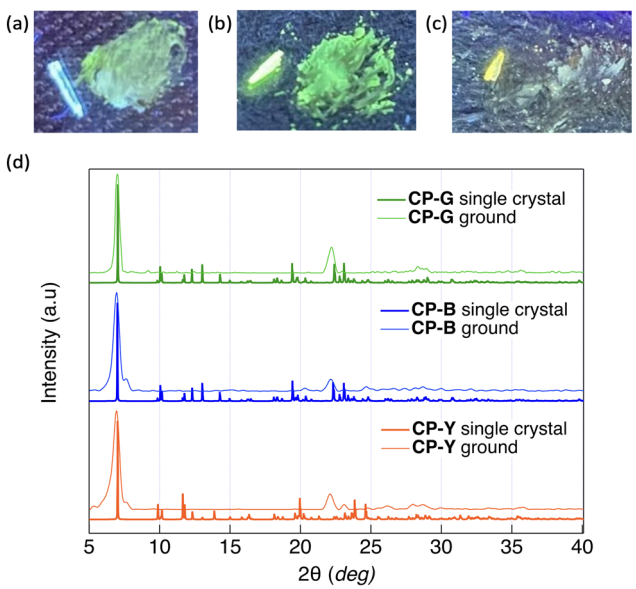

Fig. 7 Photographs of (a) **CP-B**, (b) **CP-G**, and (c) **CP-Y** before (left) and after (right) mechanical grinding under 254 nm UV irradiation. (d) Experimental powder XRD patterns of ground crystals (thin lines) and XRD patterns of bulk crystals simulated from the SCXRD structures (bold lines).

the τ value of the ground sample became shorter. This means that the RTP efficiency of the crystal is significantly quenched upon mechanical grinding; that is, the destruction of the crystal structure upon mechanical grinding promotes nonradiative deactivation, which is in good agreement with the higher k_{nr} value of the ground crystals.

The powder X-ray diffraction (PXRD) patterns of the **CP** polymorphs after mechanical grinding and corresponding patterns simulated from the SCXRD structures are shown in Fig. 7d. The crystal size of the ground samples was determined using the Scherrer equation. Both ground **CP-B** and **CP-Y** exhibited a crystal size of 15 nm, while the crystal size of ground **CP-G** was slightly larger at 26 nm. Upon grinding, **CP-B** and **CP-Y** exhibited a change in crystalline structure, which explains the origin of the MCL behaviour. Similarly, the mechanical grinding of **CP-G** also induced a crystalline structure, even though the emission colour barely changed. Upon comparison of the PXRD patterns of the ground samples, it is evident that both ground **CP-B** and **CP-Y** exhibit similar PXRD patterns, which differ from that of ground **CP-G**. Notably, ground **CP-B** and **CP-Y** both display an additional peak close to the main peak at 12.6 Å, along with a wider angle peak relative to ground **CP-G**. These findings suggest that grinding **CP** bulk crystals may lead to the formation of new crystal phases with different structures. However, it is noteworthy that despite these structural differences, the comparable Au–Au distances suggest similar luminescence profiles in all ground samples.

We indexed the PXRD patterns of bulk **CP-B** and **CP-G** based on the SCXRD data to identify whether there were subtle differences in the crystal structure that could contribute to the differences in emission colours (Fig. S16, ESI†). However, we found similar $d(hkl)$ values for both polymorphs, indicating that the structures were nearly identical and that the difference in emission colour was not caused by the different aggregated structures. Considering the presence of green-emitting $\mathbf{CP_{ground}}$ with different crystal structures, it is possible that green-emitting **CP-G** contains small crystal domains of the $\mathbf{CP_{ground}}$ polymorph, which has a different emission colour than **CP-B**. Consequently, energy transfer from the main crystal lattice (**CP-B**) to the small-crystal-domain $\mathbf{CP_{ground}}$ leads to an overall green emission in **CP-G**, even though it has the same crystal structure as **CP-B**. Theoretically, in a Förster resonant energy transfer (FRET) system, the donor moiety absorbs incident light and transfers the energy to a smaller quantity of emitter luminophores.[19] This is in accordance with the observed luminescence spectrum in **CP-G**, where the excitation spectrum mainly consists of the donor characteristics of **CP-B** as the main crystal lattice at ~320 nm, whereas the emission spectrum arises from $\mathbf{CP_{ground}}$ as an emitter at ~500 nm, resulting in an increased Stokes shift of the overall spectrum. A similar phenomenon in which a small crystal domain caused a change in overall crystal emission has been reported previously in a mechanochromic Au complex[20] and in a doped organic crystal.[21] The biexponential lifetime observed in **CP-G** can provide evidence for the presence of a $\mathbf{CP_{ground}}$ crystal domain within the bulk **CP-G** crystal. The shorter lifetime of 4 μs is likely attributable to the $\mathbf{CP_{ground}}$ crystal domain, while the longer lifetime of 389 μs is attributed to FRET from the bulk **CP-G** crystal. It is generally known that the observed Φ of a FRET system depends largely on the Φ of the emitters.[22] The reason is that **CP-G** exhibits higher Φ (23%) than **CP-B** (10%) as a donor moiety might be due to the highly emissive $\mathbf{CP_{ground}}$ crystal domain which acts as emitter in **CP-G**. The low quantum yield of $\mathbf{CP_{ground}}$ obtained through mechanical grinding is attributed to poor crystal quality, such as disorder, distortion, and inclination, which promote nonradiative deactivation. In contrast, $\mathbf{CP_{ground}}$ within the bulk **CP-G** crystal formed under slow recrystallisation and exhibits more efficient luminescence, likely because the densely packed crystal structure prevented oxygen penetration and emission quenching. The formation of a small crystal domain ($\mathbf{CP_{ground}}$) was also observed in THF/water mixed solvents with high water content, identified as band III in Fig. 3. Presently, the crystal structure of $\mathbf{CP_{ground}}$ remains unclear; however, it is postulated that aurophilic interactions with shorter Au–Au distances, compared to those present in the main **CP-B** crystal, are involved. These interactions are believed to contribute to the higher RTP quantum yields observed for **CP-G**.

Thermal phase transition behaviour

The thermal phase transition behaviour of **CP** was observed by differential scanning calorimetry (DSC) and polarised optical microscopy (POM). The DSC thermograms of all the bulk crystal polymorphs (Fig. S5, ESI†) exhibited small endothermic peaks at approximately 40 °C during the first heating process. However, the optical texture of the crystal was retained at this temperature, as observed using POM. Therefore, it can be concluded that the phase transition at 40 °C corresponds to a crystal-to-crystal phase transition, which also support the polymorphism behaviour observed in the bulk crystal. At high temperatures, **CP** exhibited an enantiotropic nematic (N) LC phase, as indicated by intense exothermic and endothermic peaks appearing during both heating and cooling. A nematic LC phase was assigned based on the optical texture observed by POM, where a schlieren texture was observed at approximately 122 °C (Fig. 8b). This N phase was retained until the T_{dec} of the complex. In general, the molecular skeleton of LCs contains a rigid core and flexible alkyl or alkoxy chains. The less rigid structure of the cyclohexyl group is likely to act as a flexible unit to aid the LC phase formation. Upon cooling from the molten states of the bulk crystals, an N-to-crystal phase transition occurs without any observed subsequent crystal-to-crystal phase transitions. This indicates that the original crystal (Cr_1) is metastable, and does not recover after its transition to the N phase.

During the first cooling process in **CP-G**, multiple exothermic peaks were observed following the N-to-crystal phase transition, which was not seen in other **CP** polymorphs. Following our previous hypothesis that **CP-G** bulk crystal contains small crystal domains similar to $\mathbf{CP_{ground}}$, we also investigated the phase transition of $\mathbf{CP_{ground}}$ (Fig. S6, ESI†). Unlike the bulk crystals, the crystal-to-crystal phase transition was not observed

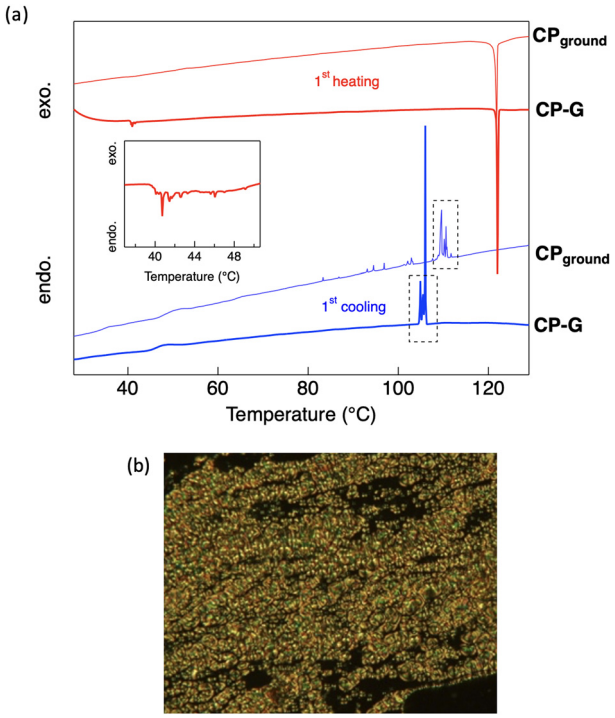

Fig. 8 (a) DSC thermograms of **CP-G** and $\mathbf{CP_{ground}}$ during the first scan and (b) POM image of **CP** showing the N phase, observed at 125 °C. The red and blue curves indicate the heating and cooling cycles, respectively. The dashed rectangles represent the region where the peaks are similar between **CP-G** and $\mathbf{CP_{ground}}$.

in $\mathbf{CP_{ground}}$ during the first heating, indicating that the original state of $\mathbf{CP_{ground}}$ is more stable, similar to the Cr_2 phase observed in **CP** crystals. In addition, cooling the molten $\mathbf{CP_{ground}}$ sample resulted in multiple unidentified crystal-to-crystal phase transitions (Fig. 8a), resembling those observed in bulk **CP-G**. Similarly, during the third scan, the phase transition of $\mathbf{CP_{ground}}$ closely matched that of bulk **CP-G** (Fig. S5b and S6, ESI†), namely, a broad endothermic peak at approximately 120 °C and exothermic peaks at ~100 °C. These support the presence of $\mathbf{CP_{ground}}$ within bulk **CP-G**. The appearance of multiple peaks in $\mathbf{CP_{ground}}$ after subsequent scans is attributed to crystal defects. These defects or changes in molecular orientation provide nucleation sites for the formation of different crystal phases, resulting in multiple crystal-to-crystal phase transitions during cooling.[23]

To study the effect of the phase transition on the luminescence behaviour, we investigated the photoluminescence spectra of **CP** polymorphs in the LC phase (Fig. S22–S29, ESI†). All **CP** polymorphs showed a decrease in the absolute luminescence intensity upon heating due to the thermal deactivation of excited states. Temperature-dependent luminescence intensity plots for **CP-B**, **CP-G**, and **CP-Y**, are shown in Fig. S24, S27, and S29 (ESI†), respectively. Initially, all polymorphs show a gradual decrease in emission intensity, which was rapidly quenched after reaching the crystal-to-crystal phase transition temperature at 40 °C. Subsequently, the emission intensity continued to decrease until the LC phase temperature was reached. The luminescence spectral shape altered upon the crystal-to-crystal phase transition: for **CP-B**, the broad shoulder peak at 500–600 nm disappeared above 40 °C (Fig. S22, ESI†); for **CP-Y**, the emission at 560 nm rapidly quenched while the emission at 424 nm persisted, resulting in a pronounced blue shift in the emission maxima (Fig. S28a, ESI†). These results indicate that the longer wavelength emission band originated from the original Cr_1 phase, and the crystal-to-crystal phase transition altered the luminescence. In contrast, **CP-G** exhibited no significant change in its emission spectral shape upon undergoing the crystal-to-crystal phase transition. Instead, heating to the N phase temperature led to a broadening emission band, where the ratio between shorter-wavelength emission (~420 nm) and the main emission at 500 nm became nearly equal (Fig. S25, ESI†). It is noteworthy that in **CP-Y**, the emission at 560 nm remained observable at 50 °C despite this temperature corresponding to the Cr_2 phase. Prolonging the holding time at 50 °C to approximately 20 min led to a reduction in the relative emission intensity at 560 nm (Fig. S28c, ESI†). This implies that some crystals did not immediately transition from Cr_1 to Cr_2 at 50 °C, which is considered to also be applicable to other **CP** polymorphs. Notably, the difference in the luminescence spectrum of **CP-Y** at room temperature in Fig. S28 (ESI†) compared to Fig. 5 is attributed to the lower quality of the crystal used in the temperature-dependent luminescence measurement. Even in high-quality crystals, **CP-Y** exhibited a shorter wavelength peak at 423 nm under excitation at 320 nm (Fig. 5). In high-quality crystals, this shorter wavelength peak is significantly lower compared to the main emission at 560 nm.

After cooling the molten sample to room temperature, all polymorphs retained only 25% of their luminescence intensity, which is attributed to less-ordered crystals. Moreover, in both **CP-B** and **CP-Y** the emission maxima of the frozen crystal (Cr_2) were red-shifted by 39 nm, and the shoulder peak at longer wavelengths was recovered (Fig. S23b and S28d, ESI†). In contrast, cooling molten **CP-G** to room temperature recovers its green emission (~500 nm) (Fig. S26, ESI†). Because the crystal-to-LC phase transition temperature is close to the T_{dec} of **CP**, the LC temperature (130 °C) was maintained for less than 5 min before the cooling process. Due to this short holding time, a small number of **CP-G** crystals might persist and not completely transition to the LC phase, resulting in continued observation of the green emission band at 500 nm even after cooling. These results suggest that the temperature-induced phase transition of **CP** polymorphs can significantly alter their luminescence behaviour.

To gain deeper insights into the thermal behaviour of the luminescence process, Arrhenius-type plots were utilised (Fig. S30, ESI†). The estimation of activation energy (E_a) for thermal quenching associated with the phase transitions of **CP** crystals was derived from the slope of these plots. Note that plots close to the phase transition temperature, with a significant margin of error, were excluded from subsequent analyses. For **CP-B** and **CP-G**, the initial slope observed during heating the sample up to 40 °C indicated E_a values of 5.5 and 13 kJ mol^{-1}, respectively. Between 40 and 50 °C, discrete changes in the plot

were observed for both polymorphs. Beyond 50 °C, the E_a values of **CP-B** and **CP-G** increased to 13 and 24 kJ mol^{-1}, respectively, until the phase transition to the LC phase. This rise in E_a between 40 and 50 °C is attributable to the crystal-to-crystal phase transition, aligning closely with the DSC results. These results indicate that alteration in the crystal packing structure affects the rate of thermal deactivation of the excited states. **CP-Y** exhibited similar behaviour under both S_0–S_n and direct S_0–T_n excitation (Fig. S30c and d, ESI†). In contrast, during cooling, a decline in the logarithm of luminescence intensity was observed in the N phase for all samples, while it remained constant in the crystal phase until approximately 80 °C (Fig. S30e–g, ESI†). We hypothesise that the transient decrease in the N phase is linked to the instability of the LC phase at temperatures close to their N-to-crystal phase transition. Subsequently, the crystals gradually grew from the N phase below the phase transition temperature. However, immediately after the phase transition temperature, a biphasic region exists until ~80 °C because the cooling rate (2 °C s^{-1}) was too rapid for crystal growth, resulting in a constant region in log intensity. The crystal domains grow during the cooling process *via* Ostwald ripening. Below 80 °C, there is a gradual increase in log emission intensity along with a change in spectral shape. These results further support the dependence of luminescence properties on polymorphism.

Conclusions

In summary, the **CP** Au complex exhibited multicolour RTP in the bulk crystal, which was attributed to its polymorphic behaviour. Three types of crystals with high-contrast luminescent colours were obtained by controlling the recrystallisation conditions. **CP** exhibited a strong RTP with Φ_{RTP} of up to 38%. The SCXRD results revealed that **CP-Y** exhibited a shorter Au–Au distance, which can explain the observed distinct luminescent colour. In contrast, **CP-B** and **CP-G** have longer Au–Au distances and identical crystal structures, despite exhibiting distinct luminescence properties. This type of polymorphism is rare, and our study revealed that the presence of a small $\mathbf{CP_{ground}}$ crystal domain was responsible for the overall green emission observed in **CP-G**. The FRET process occurs from the main crystal domain to $\mathbf{CP_{ground}}$ as an emitter. A switch in luminescent colour in **CP** can also be induced by mechanical stimuli due to alternation of the aggregated structure. Moreover, **CP** exhibited an N phase at higher temperatures, where luminescence was also observed. Our study demonstrates that the luminescence behaviour of **CP** Au complexes can be effectively controlled through crystal-to-crystal and crystal-to-LC phase transitions. Thus, we expect that this LC Au complex has great potential as a colour-controllable emitting material for applications in various optoelectronic devices.

Experimental

Materials

The Au complex **CP** was synthesised in two facile steps, as shown in Fig. 1. All solvents and reagents were of reagent grade, commercially available, and used without further purification unless otherwise noted. ^{1}H and ^{13}C NMR spectra were recorded using a JEOL ECS-400 spectrometer (^{1}H: 400 MHz and ^{13}C: 100 MHz) in $CDCl_3$. Chemical shifts are reported in parts per million (ppm), with residual protons or carbon atoms in the NMR solvent as an internal reference. IR spectra were obtained using the KBr disk method with a JASCO FT/IR-4100 spectrometer, and all spectra were reported as wavenumbers (cm^{-1}). HRMS was performed on a JEOL JMS-700 spectrometer. Elemental analysis was conducted using a MICRO CORDER JM10 apparatus (J-SCIENCE).

Synthesis of complex CP

Ethynyl-4-(*trans*-4-propylcyclohexyl)benzene (86 mg, 0.38 mmol) and (tht)AuCl (0.12 g, 0.42 mmol) were dissolved in CH_2Cl_2 (7 mL), and a freshly prepared solution of CH_3COONa (0.26 g, 1.9 mmol) in MeOH (4 mL) was added to the solution at room temperature with stirring. After stirring at room temperature for 2 h, the precipitate was collected by filtration and washed with MeOH, H_2O, and CH_2Cl_2. The obtained yellow solid was suspended in CH_2Cl_2 (15 mL), and 1-pentyl isocyanide (0.047 mL, 0.42 mmol) was added dropwise to the resultant suspension at room temperature. The reaction mixture was stirred at room temperature for 2 h, and then subjected to Celite® filtration, followed by the removal of solvent from the filtrate using a rotary evaporator. The resultant white solid was purified by silica-gel column chromatography (eluent: CH_2Cl_2), followed by recrystallization from a mixture of CH_2Cl_2 and *n*-hexane (1 : 2 v/v), yielding colourless plate crystals of **CP** in 39% yield (75 mg, 0.14 mmol) in two steps. mp 122 °C. ^{1}H NMR ($CDCl_3$, δ): 7.39 (dd, J = 6.3, 1.8 Hz; 2H; 2,6-*H* in phenyl), 7.08 (dd, J = 6.3, 1.6 Hz; 2H; 3,5-*H* in phenyl), 3.61 (t, J = 5.6 Hz; 2H; C≡NCH_2), 2.41 (m, 1H; 1-*H* in cyclohexyl), 1.83 (m, 6H; C≡NCH$_2$CH_2, and 2,3,5,6-*H* in cyclohexyl (equatorial)), 1.50–1.16 (m, 11H; 4-*H* in cyclohexyl, 1-CH_2 in propyl, C≡NCH$_2$CH$_2$(CH_2)$_2$, and 2,3,5,6-*H* in cyclohexyl (axial)), 1.09–0.89 (m, 5H; 2-CH_2 in propyl, C≡N(CH$_2$)$_4$CH_3), 0.87 (t, J = 7.2 Hz; 3H; CH_3 in propyl). ^{13}C NMR ($CDCl_3$, δ): 146.95, 132.429, 126.561, 121.920, 120.569, 103.741, 44.530, 44.051, 39.797, 37.072, 34.231, 33.604, 28.368, 27.851, 21.805, 20.110, 14.515, 13.844. FTIR (KBr, ν): 3033, 2952, 2923, 2251 cm^{-1}. HRMS (ESI, m/z): calculated for $C_{23}H_{32}AuNNa$ $(M + Na)^+$, 542.2093; found, 542.2090. Anal. calcd for $C_{23}H_{32}AuN$: C, 53.18; H, 6.21; N, 2.70; Au, 37.92. Found: C, 53.02; H, 5.91; N, 2.69; Ash, 38.1.

X-ray crystallography

Single crystals of the Au complex were obtained by slow evaporation from mixed solvents (1 : 3 v/v mixture of CH_2Cl_2 and *n*-hexane for **CP-B** and **CP-G**, and 1 : 3 v/v mixture of CH_2Cl_2 and ethyl acetate for **CP-Y**). The reflection data were collected using the omega scanning technique with a Bruker D8 goniometer. Monochromatic Mo Kα radiation (λ = 0.71075 Å) was used to analyse the complexes and all measurements were performed at ambient temperature (293 K). The initial structure of the unit cell was determined using APEX2 using direct methods. The structural model was refined by a full-matrix

least-squares method using SHELXL. The crystal structure data for **CP** are provided in the ESI.† The indexed data of **CP** complex were deposited in the Cambridge Crystallographic Data Centre (CCDC) database under reference number 2327717 (**CP-B**), CCDC 2327718 (**CP-G**), and CCDC 2327741 (**CP-Y**). The indexed database contains additional supplementary crystallographic data for this study and may be accessed without charge at **https://www.ccdc.cam.ac.uk/conts/retrieving.html** (accessed on 2024).

PXRD measurements were operated using the X' Pert PRO system (PANalytical) at 45 kV and 40 mA with Cu Kα radiation (λ = 1.5405 Å).

Thermal properties

The phase transition properties of the Au complex were observed by POM using an Olympus BX51 microscope equipped with a temperature-controlled stage (Instec HCS302 microscope hot and cold stages, and an mK1000 temperature controller). To assess thermal stability, TG–DTA was carried out using a DTG-60AH analyser (Shimadzu) at a heating rate of 5.0 °C min^{-1}. The thermodynamic parameters were determined using DSC (SII X-DSC7000) at heating and cooling rates of 1.0 °C min^{-1}. At least three scans were conducted to check reproducibility.

Photophysical properties

The UV-Vis absorption spectra were recorded using a JASCO V-550 absorption spectrophotometer. Steady-state photoluminescence spectra were recorded using a Hitachi F-7500 fluorescence spectrophotometer. Photoluminescence quantum yields were estimated using a calibrated integration sphere system (Hitachi). Photoluminescence decay profiles were recorded using a Hamamatsu Quantaurus-Tau photoluminescence lifetime measurement system (C1136-21).

Computation

All calculations were performed using DFT with the B3LYP hybrid functional and 6-311+G(d,p) (for C, H, and N atoms) and SDD (for Au atoms) basis sets in the Gaussian 16 (revision C.01) program package.[24] Single point calculations were conducted for the dimers using the conformation obtained from the crystal structure. The optimised geometry of the monomer was determined using DFT calculations at the same level of theory. The stationary points were characterised by frequency calculations to confirm the correct number of imaginary frequencies; it was confirmed that the minimum energy structures had no imaginary frequencies. The vertical excitation energies and oscillator strengths were estimated for the ten lowest transitions for the ground state equilibrium geometries using TD-DFT at the same level of theory.

Author contributions

A.F.: data curation, formal analysis, methodology, investigation, validation, and writing – original draft; M.D.: data curation, formal analysis, methodology, investigation; K.M.: formal analysis, investigation, and writing – original draft; K.H.: formal analysis, investigation, writing – review and editing. O.T.: conceptualisation, formal analysis, supervision, project administration, resources, writing – review and editing, and funding acquisition.

Conflicts of interest

The authors declare there are no conflicts of interest.

Acknowledgements

This research was supported by the Japan Science and Technology agency (JST) A-STEP program (JPMJTR22T1), the Toshiaki Ogasawara Memorial Foundation, and the Cooperative Research Program of the Network Joint Research Centre for Materials and Devices.

References

1 (*a*) C. Murawski and M. C. Gather, *Adv. Opt. Mater.*, 2021, **9**, 2100269; (*b*) S. Negi, P. Mittal, B. Kumar and P. K. Juneja, *Microelectron. Eng.*, 2019, **218**, 111154; (*c*) X. Zhang, X. Zhang, B. Yang, J. Hui, M. Liu, Z. Chi, S. Liu, J. Xu and Y. Wei, *Polym. Chem.*, 2014, **5**, 318.

2 K. Zhang, J. Liu, Y. Zhang, J. Fan, C.-K. Wang and L. Lin, *J. Phys. Chem. C*, 2019, **123**, 24705.

3 (*a*) B. Z. Tang, X. Zhan, G. Yu, P. P. Sze Lee, Y. Liu and D. Zhu, *J. Mater. Chem.*, 2001, **11**, 2974; (*b*) B. Jiang, C.-W. Zhang, X.-L. Shi and H.-B. Yang, *Chin. J. Polym. Sci.*, 2019, **37**, 372; (*c*) P. Alam, C. Climent, P. Alemany and I. R. Laskar, *J. Photochem. Photobiol., C*, 2019, **41**, 100317; (*d*) S. Suzuki, S. Sasaki, A. S. Sairi, R. Iwai, B. Z. Tang and G. Konishi, *Angew. Chem., Int. Ed.*, 2020, **59**, 9856.

4 (*a*) A. L. Balch, *Angew. Chem., Int. Ed.*, 2009, **48**, 2641; (*b*) Y. Sagara and T. Kato, *Angew. Chem., Int. Ed.*, 2011, **50**, 9128; (*c*) M.-J. Teng, X.-R. Jia, X.-F. Chen and Y. Wei, *Angew. Chem., Int. Ed.*, 2012, **51**, 6398.

5 (*a*) S. Kohmoto, R. Tsuyuki, H. Masu, I. Azumaya and K. Kishikawa, *Tetrahedron Lett.*, 2008, **49**, 39; (*b*) W. Lu, N. Zhu and C. M. Che, *J. Am. Chem. Soc.*, 2003, **125**, 16081; (*c*) G. Zhang, J. Lu, M. Sabat and C. L. Fraser, *J. Am. Chem. Soc.*, 2010, **132**, 2160.

6 (*a*) Y. Sagara and T. Kato, *Angew. Chem., Int. Ed.*, 2008, **47**, 5175; (*b*) Y. Sagara and T. Kato, *Nat. Chem.*, 2009, **1**, 605; (*c*) K. Nagura, S. Saito, H. Yusa, H. Yamawaki, H. Fujihisa, H. Sato, Y. Shimoikeda and S. Yamaguchi, *J. Am. Chem. Soc.*, 2013, **135**, 10322.

7 K. Hisano, S. Panthai and O. Tsutsumi, in *Handbook of Aggregation-Induced Emission*, ed. Y. Tang and B. Z. Tang, John Wiley & Sons Ltd., 2022, vol. 9, p. 555.

8 (*a*) T. Seki, K. Sakurada and H. Ito, *Angew. Chem., Int. Ed.*, 2013, **52**, 12828; (*b*) A. Sathyanarayana, S. Nakamura, K. Hisano, O. Tsutsumi, K. Srinivas and G. Prabusankar,

Sci. China: Chem., 2018, **61**, 957; (*c*) R. Kawano, O. Younis, A. Ando, Y. Rokusha, S. Yamada and O. Tsutsumi, *Chem. Lett.*, 2016, **45**, 66; (*d*) K. Fujisawa, S. Yamada, Y. Yanagi, Y. Yoshioka, A. Kiyohara and O. Tsutsumi, *Sci. Rep.*, 2015, **5**, 7934.

9 (*a*) K. Fujisawa, N. Kawakami, Y. Onishi, Y. Izumi, S. Tamai, N. Sugimoto and O. Tsutsumi, *J. Mater. Chem. C*, 2013, **1**, 5359; (*b*) K. Fujisawa, Y. Okuda, Y. Izumi, A. Nagamatsu, Y. Rokusha, Y. Sadaike and O. Tsutsumi, *J. Mater. Chem. C*, 2014, **2**, 3549; (*c*) S. Yamada, Y. Rokusha, R. Kawano, K. Fujisawa and O. Tsutsumi, *Faraday Discuss.*, 2017, **196**, 269.

10 (*a*) S. Roy, A. Hazra, A. Bandyopadhyay, D. Raut, P. L. Madhuri, D. S. S. Rao, U. Ramamurty, S. K. Pati, S. Krishna Prasad and T. K. Maji, *J. Phys. Chem. Lett.*, 2016, **7**, 4086; (*b*) M. Krikorian, S. Liu and T. M. Swager, *J. Am. Chem. Soc.*, 2014, **136**, 2952.

11 A. Furoida, M. Daitani, K. Hisano and O. Tsutsumi, *Molecules*, 2021, **26**, 7255.

12 (*a*) E. R. T. Tiekink and J.-G. Kang, *Coord. Chem. Rev.*, 2009, **253**, 1627; (*b*) I. O. Koshevoy, E. S. Smirnova, M. Haukka, A. Laguna, J. C. Chueca, T. A. Pakkanen, S. P. Tunik, I. Ospino and O. Crespo, *Dalton Trans.*, 2011, **40**, 7412.

13 Y. Kuroda, M. Tamaru, H. Nakasato, K. Nakamura, M. Nakata, K. Hisano, K. Fujisawa and O. Tsutsumi, *Commun. Chem.*, 2020, **3**, 139.

14 (*a*) R. C. Evans, P. Douglas and C. J. Winscom, *Coord. Chem. Rev.*, 2006, **250**, 2093; (*b*) I. E. Pomestchenko, C. R. Luman, M. Hissler, R. Ziessel and F. N. Castellano, *Inorg. Chem.*, 2003, **42**, 1394.

15 A. Ando, K. Ozaki, U. Shiina, E. Nagao, K. Hisano, K. Kamada and O. Tsutsumi, *Aggregate*, 2022, **3**, e125.

16 (*a*) L. Favereau, C. Quinton, C. Poriel, T. Roisnel, D. Jacquemin and J. Crassous, *J. Phys. Chem. Lett.*, 2020, **11**, 6426; (*b*) X. Bi, Y. Shi, T. Peng, S. Yue, F. Wang, L. Zheng and Q.-E. Cao, *Adv. Funct. Mater.*, 2021, **31**, 2101312; (*c*) O. Tsutsumi, M. Tamaru, H. Nakasato, S. Shimai, S. Panthai, Y. Kuroda, K. Yamaguchi, K. Fujisawa and K. Hisano, *Molecules*, 2019, **24**, 4606.

17 W. Shao and J. Kim, *Acc. Chem. Res.*, 2022, **55**, 1573.

18 M. Vaddamanu, A. Sathyanarayana, Y. Masaya, S. Sugiyama, O. Kazuhisa, K. Velappan, K. Subramaniyam, K. Hisano, O. Tsutsumi and G. Prabusankar, *Organometallics*, 2020, **39**, 2202.

19 B. Zhang, P. Zhao, L. J. Wilson, J. Subbiah, H. Yang, P. Mulvaney, D. J. Jones, K. P. Ghiggino and W. W. H. Wong, *ACS Energy Lett.*, 2019, **4**, 1839.

20 T. Seki, K. Sakurada and H. Ito, *Chem. Commun.*, 2015, **51**, 13933.

21 R. Yoshida, T. Tachikawa and S. Ito, *Chem. Commun.*, 2022, **58**, 6781.

22 B. Zhang, G. Lyu, E. A. Kelly and R. C. Evans, *Adv. Sci.*, 2022, **9**, 2201160.

23 (*a*) G. Shi, S. Li, P. Shi, J. Gong, M. Zhang and W. Tang, *IUCrJ*, 2021, **8**, 584; (*b*) O. Al Rahal, B. M. Kariuki, C. E. Hughes, P. A. Williams, X. Xu, S. Gaisford, D. Iuga and K. D. M. Harris, *Cryst. Growth Des.*, 2023, **23**, 3820.

24 M. J. Frisch, G. W. Trucks, H. B. Schlegel, G. E. Scuseria, M. A. Robb, J. R. Cheeseman, G. Scalmani, V. Barone, G. A. Petersson, H. Nakatsuji, X. Li, M. Caricato, A. V. Marenich, J. Bloino, B. G. Janesko, R. Gomperts, B. Mennucci, H. P. Hratchian, J. V. Ortiz, A. F. Izmaylov, J. L. Sonnenberg, D. Williams-Young, F. Ding, F. Lipparini, F. Egidi, J. Goings, B. Peng, A. Petrone, T. Henderson, D. Ranasinghe, V. G. Zakrzewski, J. Gao, N. Rega, G. Zheng, W. Liang, M. Hada, M. Ehara, K. Toyota, R. Fukuda, J. Hasegawa, M. Ishida, T. Nakajima, Y. Honda, O. Kitao, H. Nakai, T. Vreven, K. Throssell, J. A. Montgomery, Jr., J. E. Peralta, F. Ogliaro, M. J. Bearpark, J. J. Heyd, E. N. Brothers, K. N. Kudin, V. N. Staroverov, T. A. Keith, R. Kobayashi, J. Normand, K. Raghavachari, A. P. Rendell, J. C. Burant, S. S. Iyengar, J. Tomasi, M. Cossi, J. M. Millam, M. Klene, C. Adamo, R. Cammi, J. W. Ochterski, R. L. Martin, K. Morokuma, O. Farkas, J. B. Foresman and D. J. Fox, *Gaussian 16, Revision C.01*, Gaussian, Inc., Wallingford CT, 2019.